Photon-assisted transport through quantized energy states in a lateral dual-gate device

S. Verghese, R. A. Wyss, Th. Schäpers,* and Qing Hu
Department of Electrical Engineering and Computer Science, and Research Laboratory of Electronics, Massachusetts Institute of Technology, Cambridge, Massachusetts 02139-4307

A. Förster
Institut für Schicht- und Ionentechnik (ISI), Forschungszentrum Jülich, Jülich D-52428, Germany

M. J. Rooks
National Nanofabrication Facility, Cornell University, Ithaca, New York 14853-5403
(Received 12 May 1995)

We present data that are consistent with photon-assisted transport in a mesoscopic device through quantized energy states that result from lateral confinement. Two parallel gates that are orthogonal to the current flow were used to quantize a two-dimensional electron gas in a modulation-doped $Al_xGa_{1-x}As$-GaAs heterostructure with a quantization energy $\sim$ 1 meV. Photons with energies 0.37 and 1.1 meV were antenna coupled to the drain and source. The photoinduced current plotted as a function of the drain-source voltage exhibits distinctly frequency-dependent features that agree with a theoretical model based on photon-assisted transport.

Quantum-size effects lead to energy quantization when electrons travel ballistically in a potential that is modulated on the length scale of the Fermi wavelength. Mesoscopic devices, which confine electrons laterally, can exhibit both quantum-size effects and semiclassical effects, due to single-electron charging on an energy scale of roughly $0.1-1$ meV. Both of these effects have been measured electrically, but few long-wavelength optical measurements exist. Far-infrared measurements on large arrays of quantum dots have yielded information about the collective motion of charge.[1] At microwave frequencies, evidence exists for photon-assisted tunneling through states produced by single-electron charging effects in both metal[2] and semiconductor[3] dots. This paper reports evidence for photon-assisted transport in a mesoscopic device through states produced solely by quantum-size effects. The results indicate that the electron wave function preserves its phase coherence as it traverses our lateral double-barrier structure and simultaneously absorbs a photon. The experimental data are compared to a model based on photon-assisted transport, which accounts for the energy-dependence of electron transmission through the barriers.

A theoretical model for photon absorption in a mesoscopic device motivated our design. Photon absorption requires a momentum transfer of $\Delta k \approx \frac{m^*\omega}{\hbar k_f}$, for an electron of mass m^*, with wave vector $\sim k_f$ to absorb a photon with $k \approx 0$. The device described here achieves Δk transfer by spatially localizing both the electron wave function and the photon field in one dimension that is parallel to the photon's polarization. In a similar fashion, electron localization provides the required Δk for infrared detectors fabricated from vertical quantum wells.[4] These devices absorb photons when a one-dimensional (1D) localized electron in a bound state is excited into the continuum. Superconductor-insulator-superconductor junctions, however, localize the photon field roughly within a London penetration depth of the barrier region, so that transitions between extended quasiparticle states can be excited.[5] Calculations by Yakubo *et al.* suggest that both electron localization and photon localization play a role in supplying Δk in a lateral mesoscopic device.[6] The lack of a quasibound state in a quantum point contact in the direction of current flow may explain the difficulty in measuring photon-assisted transport in such systems.[7,8]

The dual-gate field-effect transistor (FET) was fabricated using a modulation-doped $Al_xGa_{1-x}As$-GaAs heterostructure.[9] The two-dimensional electron gas (2DEG) is 55 nm below the sample surface, with mobility 1.8×10^5 cm^2 V s measured at 77 K and with an electron concentration of 3.6×10^{11} cm^{-2} at 77 K. Figures 1(a) and 1(b) show a side section view and the top view of the FET. Four outer gates define the channel width to be approximately 3 μm. The 250-nm spacing of the parallel gates quantizes the electron wave function in the longitudinal dimension (electric-field direction). The ac current couples capacitively to the 2DEG and therefore avoids resistive heating at the Ohmic contacts. All gate leads are perpendicular to the antenna polarization, so that they minimally perturb the antenna pattern. During measurement, the chip was mounted on a sapphire hyperhemispherical lens, annealed at 4.2 K for $\sim$ 72 h (during which some carriers were lost from the 2DEG), until the threshold voltages V_{ng}, V_{wg} stabilized, and was finally cooled to $\sim$ 500 mK in a ^{3}He cryostat. Radiation enters the cryostat quasioptically and passes through a

0163-1829/95/52(20)/14834(5)/$06.00

vacuum window, a cold low-pass filter, and the hyperhemisphere before coupling to the planar bow tie antenna. The dc current was measured from the voltage drop across a cold 10-kΩ load resistor with a low-noise FET amplifier. The photoinduced current ΔI_{ds} was measured using a lock-in technique at 10 Hz by chopping the output of a Gunn oscillator and of a frequency tripler, and then monitoring the change in I_{ds}. We confirmed the integrity of our millimeter-wave geometry by measuring the cross-polarized signal with the radiation polarization parallel to the gates. This polarization cannot excite the photon-assisted transport process. The resulting ΔI_{ds} was reduced by a factor of 20 compared to the current induced with a longitudinally polarized field for which photon-assisted transport can occur.

Figure 1(c) shows numerical solutions of the Poisson equation for the conduction band profile for the geometry shown in the upper inset.[10] Figure 1(d) shows the transmission coefficient $T(\epsilon)$ calculated using a transfer matrix method.[11] The energies of the quasibound states are identified by the peaks in $T(\epsilon)$, whose widths give the traversal time τ for transport through these states. The energy spacing between the quasibound states is ~ 1 meV and τ for these states decreases exponentially with increasing energy. The sharp transmission peak at 10 meV in $T(\epsilon)$ corresponds to an occupied state just below the Fermi energy E_f. The wider peak at 11 meV corresponds to a quasibound state, which lies above the wide barrier, but below the narrow barrier. At 12 meV, the small undulation in $T(\epsilon)$ results from a short-lived virtual state lying above both barriers. Above 12 meV, the barriers are transparent and there is a continuum of propagating states.

Figure 2(a) shows data for the drain-source current I_{ds} plotted as a function of the voltage applied to the narrow gate V_{ng} and to the wide gate V_{wg}, both with respect to the source. A relatively small drain-source voltage

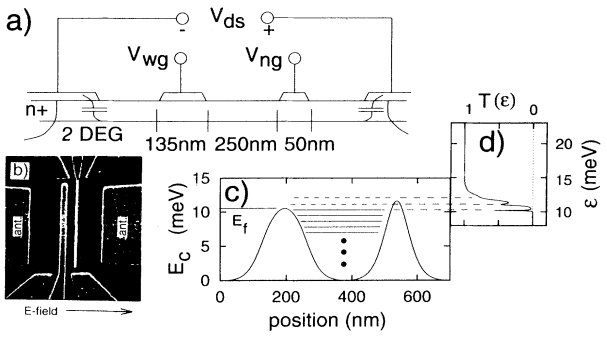

FIG. 1. (a) Schematic side view of the dual-gate FET. (b) Electron micrograph of a top view of the FET. Antenna terminals and the electric-field direction are indicated. (c) Conduction band profile calculated for $V_{ng} = -0.135$ V and $V_{wg} = -0.065$ V, from the Poisson equation (Ref. 10). (d) Calculated transmission coefficient $T(\epsilon)$. Quantized states in the barrier region are separated by ~ 1 meV. The ellipsis represents the rest of the states.

$V_{ds} = 100\,\mu$V was used to probe the transmission coefficient without distorting the barriers significantly. When both gates are biased near the pinch-off region, a shallow dip appears with a negative transconductance dI_{ds}/dV_{ng}. Calculations of $T(\epsilon)$ suggest that this feature is due to the virtual level at 12 meV, which is above both barriers as indicated in Fig. 1(c). However, calculations of the energy and linewidth of the virtual state from these data are unreliable without detailed knowledge of the parasitic capacitances and trapped charge, which affect the coupling of the gate voltages to the 2DEG. The observed shifts in the threshold voltages during the anneal at 4.2 K exemplify the difficulty of calculating this coupling accurately. Figure 2(b) shows data for I_{ds} plotted as a function of V_{ds}, where V_{wg} is fixed and V_{ng} is incremented in 5-mV steps. The overall shape of the curves is consistent with thermionic emission over a barrier. There is an asymmetry in V_{ds} for the $I_{ds} - V_{ds}$ curves that probably results from a polarity-dependent distortion of the asymmetric barriers.

If we neglect the distortion of the barriers by V_{ds}, we can calculate the dc $I_{ds}-V_{ds}$ characteristic from the curve

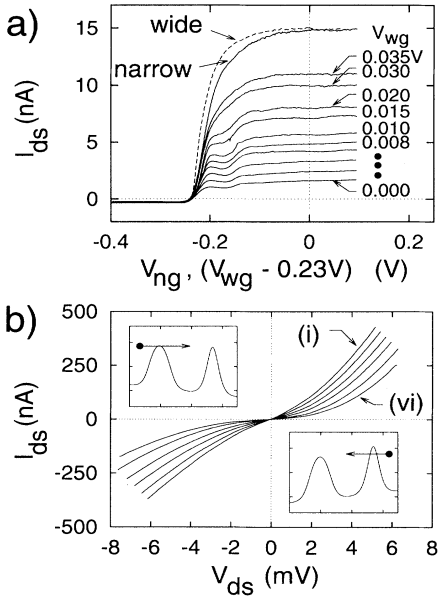

FIG. 2. (a) Drain-source current I_{ds} plotted versus gate voltage with a drain-source voltage $V_{ds} = 100\,\mu$V. Wide: I_{ds} plotted against the wide-gate voltage V_{wg} with V_{ng} at a voltage where the barrier, due to the narrow gate, is negligible. Because of an anomalously high threshold voltage, due to charge trapping, the curve has been shifted by -0.23 V for comparison with the narrow gate. Narrow: I_{ds} plotted versus V_{ng} with the barrier due to V_{wg} negligible. Other curves: I_{ds} plotted versus V_{ng} with fixed values of V_{wg}. (b) I_{ds} versus V_{ds} for $V_{wg} = 0.006$ V and for fixed values of V_{ng} decreased by 5 mV from -0.215 V in curve (i) to -0.240 V in curve (vi). The insets illustrate the asymmetry in V_{ds} of the potential profile imposed by barrier distortion.

for $T(\epsilon)$ shown in Fig. 1(d). After integration over a 1D density of states for the transverse energies, the dc result is

$$I_{ds}(V_0) = \frac{eL(2m^*)^{1/2}}{h^2} \int d\epsilon \left[F_{-1/2}\left(\epsilon - \frac{eV_0}{2} - E_f\right) - F_{-1/2}\left(\epsilon + \frac{eV_0}{2} - E_f\right)\right] T(\epsilon) \,, \quad (1)$$

where L is the transverse dimension of the FET, m^* is the electron effective mass, $F_{-1/2}$ is the Fermi-Dirac integral,[12] and V_0 is the dc value of V_{ds}. The inset in Fig. 3(b) shows the calculated $I_{ds} - V_{ds}$ curve resulting from Eq. (1) and the measured $I_{ds} - V_{ds}$ curve shown in Fig. 2(b) (*iv*). The curves agree in shape but not in magnitude, possibly because of effects such as inhomogeneity of the barriers in the transverse dimension.

Once the photon field couples to the states in the FET, its effect can be modeled as an ac voltage $V(t)$ between the drain and source in the perturbative Hamiltonian. For an ac voltage $V(t) = V_1 \cos(\omega t)$, propagating electron wave functions on the left and right side of the barriers will differ by a phase factor $\exp(ieV_0t/\hbar)[\sum_n J_n(\alpha) \exp(in\omega t)]$, where $\alpha \equiv eV_1/\hbar\omega$.[5] Using the formalism originally developed by Werthamer[13,14] and changing variables, one can show that the effect of the phase factor on the dc I_{ds}–V_{ds} curve can be lumped into an effective transmission coefficient $T_\omega(\epsilon)$, which replaces $T(\epsilon)$ in Eq. (1).[15] In the limit $\alpha \ll 1$, only single-photon processes contribute to the current $I_{ds}(V_0, V_1(\omega))$ and

$$T_\omega(\epsilon) \equiv (\alpha^2/4)T(\epsilon + \hbar\omega/2) + (1 - \alpha^2/2)T(\epsilon) + (\alpha^2/4)T(\epsilon - \hbar\omega/2) \,. \quad (2)$$

Equation (2) and Fig. 3(a) show that the radiation field effectively produces two sidebands for each transmission peak in $T(\epsilon)$ which, for an electron, correspond to either absorption or emission of a photon of energy $\hbar\omega$. The factor of 1/2, which multiplies $\hbar\omega$, is a consequence of our requirement that $V_{ds} = V_0 + V_1(t)$ drops symmetrically between drain and source.

In the presence of radiation, there are two regimes of transport that are separated by a crossover frequency $\omega_0 \approx \tau^{-1}$, where τ is the traversal time through the double-barrier region.[15] Adiabatic transport occurs when $\omega \ll \tau^{-1}$ and measurements of ΔI_{ds} for $\omega \ll \tau^{-1}$ only provide information that is already contained in the dc I_{ds}–V_{ds} curve. In the photon-assisted transport regime where $\omega > \tau^{-1}$, the electron interacts with the barrier region long enough to absorb or emit a photon and the shape of I_{ds}–V_{ds} depends on ω. At 90 GHz, we estimate that $\omega\tau \approx 7$ for the sharp state ($\tau \approx 12$ ps) at 10 meV in Fig. 1(d) and $\omega\tau \approx 1.2$ for the quasibound state just above E_f ($\tau \approx 2$ ps). Therefore, structure associated with these states should result from photon-assisted transport.

The details of barrier distortion produced the sharpest features in the experimental ΔI_{ds} data for $V_{ds} > 0$. Since the model does not include barrier distortion, it is symmetric in V_{ds} and we only compare data for $V_{ds} > 0$ to the model. The four curves in Fig. 3(b)(*i*) at 90 GHz and 3(c) (*i*) at 270 GHz show experimental data for the photoinduced current $\Delta I_{ds} \equiv I_{ds}(V_0, V_1(\omega)) - I_{ds}(V_0)$. The curves are offset at increments of 5 nA, as described in the caption. From top to bottom, the four curves use the same gate voltages, respectively, as curves (*i*)–(*iv*) in Fig. 2(b). The power from both sources was strongly attenuated in order to keep $\alpha \lesssim 1$. At such low power, the magnitude of the photocurrent depended approximately linearly on the power and the shapes of the photocurrent curves were independent of power. The changes in shape

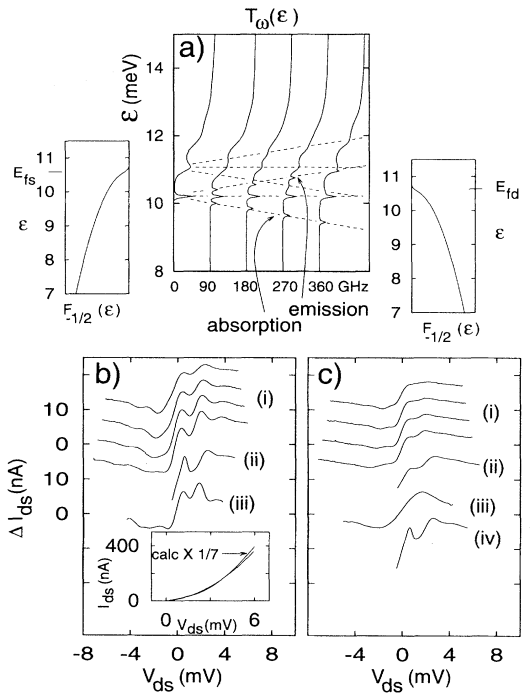

FIG. 3. (a) The effect on $T(\epsilon)$ in Fig. 1(d) of an ac voltage applied between drain and source calculated for $\alpha = 1$. For $\omega > \tau^{-1}$, sidebands appear in $T(\epsilon)$, which are associated with photon-assisted transport. The resulting dc current is calculated by integrating $T_\omega(\epsilon)$ with the left- and right-side electron distributions. (b) 90 GHz data and calculations. (c) 270 GHz data and calculations. Both (b) and (c) Curve (*i*): Four curves of the measured photocurrent ΔI_{ds} with gate voltages from top to bottom corresponding to curves (*i*)–(*iv*), respectively, in Fig. 2(b). The zero in ΔI_{ds} for the bottom curve of (*i*) is that shown to the immediate left of the curve. The other three curves in (*i*) are displaced from that zero in increments of 5 nA. Curve (*ii*): Calculated ΔI_{ds} at both frequencies using the microscopic model shown in (a). Curve (*ii*) is displaced by 10 nA from the zero shown for curve (*iii*). Curve (*iii*): Calculated ΔI_{ds} at both frequencies, using a model based on the experimental $I_{ds} - V_{ds}$ curve. (c) Curve (*iv*): Bolometric ΔI_{ds} obtained by using Eq. (1) to calculate the difference in $I_{ds}(V_0)$ at 1.2 K and 0.5 K. This calculation is independent of frequency and cannot explain the 270 GHz data. (b) Inset: Comparison of a calculated I-V curve with a measured curve.

of the four curves from 90 GHz to 270 GHz are strong evidence for photon-assisted transport. Classical effects, such as rectification or bolometric response, would not exhibit this frequency dependence. Warming the FET to 2 K completely washed out the sharp features in curves (*i*).

For the parallel-gate FET, sharp photonic features that scale with voltage in proportion to $\hbar\omega/e$ do not appear in the ΔI_{ds} data. Such features do appear in the calculated transmission coefficient $T_\omega(\epsilon)$ shown in Fig. 3(a). When $T_\omega(\epsilon)$ is convolved with the single-particle distribution functions in Eq. (1), the sidebands predominantly cause the widths of the peaks and valleys in ΔI_{ds} to differ at 90 GHz and 270 GHz. The peaks and valleys do not shift appreciably in V_{ds}. This effect has been verified theoretically for a transmission coefficient with much sharper resonant features than that shown in Fig. 3(a).[16]

For brevity, we only compare the bottom curve in Fig. 3(b) (*i*) and 3(c) (*i*) to model calculations of the photocurrent. Curve (*ii*) in Fig. 3(b) and 3(c) is a microscopic calculation of ΔI_{ds} for 90 GHz and 270 GHz, using Eqs. (2) and (1). It qualitatively reproduces the main features of the data using only the device geometry and assumptions for the Fermi energy and coupled gate voltages. At these frequencies, the calculated device impedance was $R_\omega \sim 8\,\mathrm{k}\Omega$, the antenna impedance was $\sim 75\ \Omega$, and the calculated absorbed power was 16 pW at both frequencies ($\alpha \approx 1$ at 90 GHz, and $\alpha \approx 0.3$ at 270 GHz).[17] According to Eq. (2) and Fig. 3(a), each peak in the ΔI_{ds} data at 90 GHz corresponds to enhanced transport through a single energy state, due to photon absorption. The valleys result from the suppression of transport, which occurs when photons depopulate the original transmission peak. At 270 GHz, $\hbar\omega$ exceeds the 1 meV separation of the energy states and the photons can excite transitions between source and drain through two adjacent energy states. This effect is depicted in Fig. 3(a), by the crossing of adjacent sidebands in $T_\omega(\epsilon)$ near $\omega/2\pi = 240\,\mathrm{GHz}$. The features in the 270 GHz data are, therefore, less distinct than at 90 GHz ($\hbar\omega = 0.37\,\mathrm{meV}$), since the photocurrents through two adjacent energy states are superposed. The good agreement between the calculated and measured curves suggests that the actual transmission coefficient of the device agrees with the calculation of $T(\epsilon)$ shown in Fig. 1(d).

The calculated bolometric response [curve (*iv*) in Fig. 3(c)] resembles the calculated photonic response for $\omega \lesssim 90\,\mathrm{GHz}$.[7] The steplike structure at 270 GHz in both the data and the photonic calculation, however, differs sharply from the calculated bolometric response. Furthermore, the amplitude of the ΔI_{ds} data is lower at 270 GHz than at 90 GHz, but the features in ΔI_{ds} at 270 GHz appear less sharply. This trend contradicts the trend predicted for bolometric heating—in the bolometric model, the smaller amplitude at 270 GHz would correspond to a lower temperature increase that should result in even sharper features.

As an alternative to the microscopic calculation, ΔI_{ds} can be calculated from the measured I_{ds}–V_{ds} curve,[18,19] with only the absorbed power $P(\omega)$ as an input parameter. Combining Eqs. (2) and (1) gives

$$\Delta I_{ds} = \frac{e}{2\hbar\omega}\frac{I_{ds}(V_0+\hbar\omega/e) - 2I_{ds}(V_0) + I_{ds}(V_0-\hbar\omega/e)}{I_{ds}(V_0+\hbar\omega/e) - I_{ds}(V_0-\hbar\omega/e)} \times P(\omega)\,. \tag{3}$$

Curves (*iii*) in Figs. 3(b) and 3(c) show ΔI_{ds} calculated at 90 GHz and 270 GHz using curve (*iv*) in Fig. 2(b) and assuming an absorbed power of 16 pW. At 90 GHz, the curve calculated from Eq. (3) reproduces the features in the measured ΔI_{ds} data. This calculation also reproduces the small positive photovoltaic current that appears in the data for $V_{ds} = 0$. The photovoltaic current is caused by the nonzero curvature at $V_{ds} = 0$ for the measured $I_{ds} - V_{ds}$ curve. At 270 GHz, the curve calculated from Eq. (3) shows a poor resemblance to both the measured ΔI_{ds} and to the ΔI_{ds} from the microscopic calculation. We attribute the disagreement at 270 GHz to barrier distortion. At this high frequency, a small number of photoexcited electrons see a different barrier profile than the entire reservoir sees at a dc bias of $V_0 \pm \hbar\omega/e$. In principle, the single-particle transmission function at V_0 could be extracted from a measurement of ΔI_{ds} as a continuous function of ω. In this aspect, the photon-assisted transport measurement reveals additional information compared to the dc $I_{ds} - V_{ds}$ measurement.

In summary, measurements of the photoinduced current in a dual-gate FET are consistent with photon-assisted transport through discrete states formed by quantum-size effects. Measurements at 90 GHz and 270 GHz agree with a microscopic model for the dual-gate FET. At high frequencies, photon-assisted transport probes states above and below the Fermi energy and properties such as the lifetime of these states might be measured more accurately than from dc transport measurements alone.

We acknowledge valuable discussions with S. Feng, M. A. Kastner, C. A. Mears, and D. E. Prober. This work was supported in part by the MRSEC program of the National Science Foundation under Award No. DMR-9400334, and by MIT Lincoln Laboratory under Grant No. BX-5464.

* Present address: Institut für Schicht- und Ionentechnik (ISI), Forschungszentrum Jülich, Jülich D-52428, Germany.

[1] A. Lorke, J. P. Kotthaus, and K. Ploog, Phys. Rev. Lett. **64**, 788 (1990); Ch. Sikorski and U. Merkt, *ibid.* **62**, 2164 (1989); T. Demel, D. Heitman, P. Granbow, and K. Ploog, *ibid.* **64**, 788 (1990).

[2] J. M. Martinis, M. Nahum, and H. D. Jensen, Phys. Rev. Lett. **72**, 904 (1994); J. M. Martinis and M. Nahum, Phys. Rev. B **48**, 18 316 (1993); J. M. Hergenrother, J. G. Lu, M. T. Tuominen, D. C. Ralph, and M. Tinkham, Phys. Rev. B **51**, 9407 (1995).

[3] L. P. Kouwenhoven, S. Jauhar, K. McCormick, D. Dixon,

P. L. McEuen, Yu. V. Nazarov, N. C. van der Vaart, and C. T. Foxon, Phys. Rev. B **50**, 2019 (1994); L. P. Kouwenhoven, S. Jauhar, J. Orenstein, P. L. McEuen, Y. Nagamune, J. Motohisa, and H. Sakaki, Phys. Rev. Lett. **73**, 3443 (1994).

[4] For a review, see *Intersubband Transitions in Quantum Wells*, edited by E. Rosencher, B. Vinter, and B. F. Levine (Plenum, New York, 1992).

[5] P. K. Tien and J. P. Gordon, Phys. Rev. **129**, 647 (1963).

[6] K. Yakubo, S. Feng, and Q. Hu (unpublished).

[7] R. A. Wyss, C. C. Eugster, J. A. del Alamo, and Q. Hu, Appl. Phys. Lett. **63**, 1522 (1993); R. A. Wyss, C. C. Eugster, J. A. del Alamo, M. J. Rooks, M. R. Melloch, and Q. Hu, *ibid.* **66**, 1144 (1995).

[8] S. Feng and Q. Hu, Phys. Rev. B **48**, 5354 (1993).

[9] K. Ismail, D. A. Antoniadis, and H. I. Smith, Appl. Phys. Lett. **55**, 589 (1989); S. Y. Chou, D. R. Allee, R. F. W. Pease, and J. S. Harris, Jr., *ibid.* **55**, 589 (1989).

[10] We thank G. L. Snider for use of his two-dimensional Poisson solver.

[11] J. M. Bigelow and J.-P. Leburton, J. Appl. Phys. **76**, 2887 (1994).

[12] $F_{-1/2}(\eta) = \int_0^\infty d\epsilon_t\, \epsilon_t^{-1/2}\{1 + \exp[(\epsilon_t + \eta)/kT]\}^{-1}$. For a review, see J. S. Blakemore, Solid State Electron. **25**, 1067 (1982).

[13] N. R. Werthamer, Phys. Rev. **147**, 255 (1966).

[14] P. S. S. Guimarães, B. J. Keay, J. P. Kaminski, S. J. Allen, P. F. Hopkins, A. C. Gossard, L. T. Florez, and J. P. Harbison, Phys. Rev. Lett. **70**, 3792 (1993).

[15] M. Büttiker and R. Landauer, Phys. Rev. Lett. **82**, 1739 (1982).

[16] R. A. Wyss, Ph.D. thesis, Massachusetts Institute of Technology, 1995.

[17] The absorbed power is $\sim V^2/R_\omega$, where $R_\omega = \frac{\hbar\omega}{e}[I_{\rm ds}(V_0 + \frac{\hbar\omega}{e}) - I_{\rm ds}(V_0 - \frac{\hbar\omega}{e})]^{-1}$. Small corrections ($< 3\%$), due to multiphoton processes, are included in the 90 GHz calculation.

[18] J. R. Tucker and M. J. Feldman, Rev. Mod. Phys. **57**, 1055 (1985).

[19] S. Verghese, C. Karadi, C. A. Mears, J. Orenstein, P. L. Richards, and A. T. Barfknecht, Appl. Phys. Lett. **64**, 915 (1994).